PCCP

PAPER

View Article Online
View Journal | View Issue

Cite this: *Phys. Chem. Chem. Phys.*, 2014, **16**, 23819

Synthesis of Cr and La-codoped $SrTiO_3$ nanoparticles for enhanced photocatalytic performance under sunlight irradiation†

Surendar Tonda,[a] Santosh Kumar,[a] Oruganti Anjaneyulu[b] and Vishnu Shanker*[a]

Received 7th July 2014,
Accepted 17th September 2014

DOI: 10.1039/c4cp02963a

www.rsc.org/pccp

In this study, we report a facile polymeric citrate strategy for the synthesis of Cr,La-codoped $SrTiO_3$ nanoparticles. The synthesized samples were well characterized by various analytical techniques. The UV-vis DRS studies reveal that the absorption edge shifts towards the visible light region after doping with Cr, which is highly beneficial for absorbing the visible light in the solar spectrum. More attractively, codoping with La exhibits greatly enhanced photocatalytic activity for the degradation of Rhodamine B under sunlight irradiation. The optimum photocatalytic activity at 1 atom% of Cr,La-codoped $SrTiO_3$ nanoparticles is almost 6 times higher than that of pure $SrTiO_3$ nanoparticles and 3 times higher than that of Cr-doped $SrTiO_3$ nanoparticles. The high photocatalytic performance in the present photocatalytic system is due to codoping with La, which acts as a most effective donor for stabilizing Cr^{3+} in Cr,La-codoped $SrTiO_3$ nanoparticles. More importantly, the synthesized photocatalysts possess high reusability. A proposed mechanism for the enhanced photocatalytic activity of Cr,La-codoped $SrTiO_3$ nanoparticles was also investigated by trapping experiments. Therefore, our results not only demonstrate the highly efficient visible light photocatalytic activity of the Cr,La-codoped $SrTiO_3$ photocatalyst, but also enlighten the codoping strategy in the design and development of advanced photocatalytic materials for energy and environmental applications.

Introduction

For the sustainable development of human society, developing both alternative clean energy supplies and pollution-free technologies for environmental remediation is an urgent task. Among the wide variety of renewable energy strategies underway, semiconductor photocatalysis has emerged as one of the most promising technologies because it represents an easy way to utilize the solar energy or artificial indoor illumination, and is thus abundantly available everywhere in the world.[1–4] For efficient solar energy conversion, visible light responsive photocatalysts are important because around 45% of the whole solar energy is visible light while only 4% is UV light.[5,6] Since the discovery of hydrogen production through photoinduced water splitting on titanium dioxide (TiO_2),[6] the photocatalytic properties of various metal oxide semiconductors have been extensively studied. The metal oxides such as SnO_2, ZnO and $SrTiO_3$ have a wide band gap and possess suitable band structures to act as photocatalysts. An ideal visible light responsive photocatalyst is required to have not only a small band gap energy but also proper positions of the valence band and conduction band edges for oxidation and reduction reactions of water and organic molecules.[7]

Among the vast majority of active metal oxide photocatalysts, the perovskite strontium titanate ($SrTiO_3$) is a promising photocatalyst because of several advantages, such as a high chemical stability and an abundance of constituent elements. It has been regarded as one of the most efficient photocatalysts for water splitting and photodegradation of organic pollutants due to its strong catalytic activity, high photochemical stability, and good biological compatibility.[8–10] Moreover, when compared to the well known semiconductor photocatalyst TiO_2, the conduction band and valence band edges of $SrTiO_3$ are 200 mV more negative, a favorable feature for efficient photoelectrochemical water splitting without an applied bias.[11–13] However, the photoabsorption range of $SrTiO_3$ is restricted to UV light because it has a large energy gap of about 3.2 eV that hinders the efficiency of solar-energy conversion. Doping foreign elements into wide band gap semiconductors is an effective method being employed for the extension of light absorption into the visible region. Many efforts have therefore been made to reduce the energy gap of $SrTiO_3$.[14–16] It was found that chromium (Cr) doping is an effective way to shift the light absorption, because the occupied Cr^{3+} level is usually 2.2 eV lower than the conduction band

[a] *Department of Chemistry, National Institute of Technology Warangal, Warangal-506004, Telangana, India. E-mail: vishnu@nitw.ac.in; Fax: +91-870-2459547; Tel: +91-870-2462675*

[b] *Department of Chemistry, Indian Institute of Technology Delhi, New Delhi-110016, India*

† Electronic supplementary information (ESI) available. See DOI: 10.1039/c4cp02963a

bottom formed by the Ti 3d orbital or 1.0 eV higher than the valence band top formed by the O 2p orbital.[17] Unfortunately, the photocatalytic activity was enhanced by the presence of the Cr^{3+} charge state, but diminished by the presence of Cr^{6+}, probably due to the formation of defects in the crystal, for example the oxygen vacancy, which usually acts as a recombination center of the photogenerated electron–hole pairs.[18–20] Therefore, the stabilization of Cr^{3+} is a key strategy for enhancing the photocatalytic performance of Cr-doped photocatalysts. To resolve this problem, codoping is a promising method to suppress the formation of defects and to maintain the charge balance.[21–23] Some experimental reports showed that the photocatalytic performance of Cr-doped $SrTiO_3$ is improved by codoping with Sb^{5+}, and Ta^{5+} or Nb^{5+}.[15,24] Recently, Ouyang *et al.*[25] found that the Cr and La-codoped $SrTiO_3$ showed an enhanced photocatalytic performance in H_2 evolution. However, the photocatalytic activity and pathway of Cr and La-codoped $SrTiO_3$ for the degradation of organic pollutants remains unclear.

In the present study, we report the synthesis of Cr and La-codoped $SrTiO_3$ nanoparticles *via* a polymeric citrate precursor method. The synthesized photocatalysts were characterized by various analytical techniques. The photocatalytic activities were evaluated by studying the degradation of Rhodamine B (RhB), a water contaminant, under sunlight irradiation. Furthermore, the effect of doping on the physico-chemical properties and on the photocatalytic activities of the synthesized catalysts has been investigated in detail. Based on the experimental results, a possible photocatalytic mechanism for the degradation of RhB over Cr and La-codoped $SrTiO_3$ nanoparticles under sunlight irradiation was discussed. To the best of our knowledge, there is no report on the synthesis of Cr and La-codoped $SrTiO_3$ nanoparticles by a facile polymeric citrate route for the photocatalytic degradation of RhB under sunlight.

Experimental details

Materials

Titanium isopropoxide (Sigma-Aldrich, 99.9%), strontium nitrate (SRL, 99.0%) chromium nitrate nonahydrate (SRL, 99.0%), lanthanum nitrate hexahydrate (SRL, 99.0%), citric acid (Merck, AR grade), Rhodamine B (Sigma-Aldrich, 95.0% dye content), terephthalic acid (Merck, AR grade), *tert*-butyl alcohol (Merck, AR grade), and ammonium oxalate (Merck, AR grade) were used as received. All other reagents used in this work were of analytically pure grade and used without further purification. All aqueous solutions were prepared with doubly distilled water.

Method

The various $SrTiO_3$ samples were synthesized by a polymeric citrate precursor method (Fig. S1, ESI†). A typical procedure was carried out as follows: 3.26 mL of titanium isopropoxide was dissolved in 25 mL of ethylene glycol for about 30 min under a N_2 atmosphere at room temperature. While the solution was continuously stirred, 20.82 g of citric acid was added and stirred until complete dissolution of the reagents. To this solution, the required amount of strontium nitrate (Sr : Ti = 1 : 1) was added slowly until it became transparent. However, for the preparation of the Cr and La-codoped strontium titanate $Sr_{1-x}La_xTi_{1-x}Cr_xO_3$ (x = 0.005, 0.01, 0.015 and 0.02) nanoparticles, the stoichiometric amount of chromium nitrate nonahydrate and lanthanum nitrate hexahydrate along with strontium nitrate was added. The reaction mixture was subsequently stirred for a few minutes to achieve the complete dissolution of reagents, and then heated at around 120 °C for 5 h to promote polymerization. After heating and evaporation of the solvents, the reaction mixture gelled into a transparent brown resin. The formed resin was charred at 350 °C for 3 h with a slow heating rate and then ground to obtain a fine powder. Subsequently, the resulting powders were calcined at 800 °C for 6 h. The color of the synthesized pure $SrTiO_3$ powder was white, whereas the Cr,La-codoped $SrTiO_3$ samples were yellow. The obtained pure $SrTiO_3$ powder was denoted as STO and the obtained 0.5 to 2 atom% Cr,La-codoped $SrTiO_3$ samples were denoted as Cr,La-STO-0.5, Cr,La-STO-1.0, Cr,La-STO-1.5 and Cr,La-STO-2.0, respectively.

Characterization

X-ray diffraction (XRD) patterns were recorded on a Bruker AXS D8 Advance X-ray diffractometer using a Ni filtered Cu Kα (λ = 1.5406 Å) radiation source. UV-vis diffuse reflectance spectra (UV-vis DRS) were obtained on a THERMO Scientific Evolution 600 diffuse reflectance sphere, and $BaSO_4$ was used as a reference standard. Fourier transform infrared (FT-IR) spectra were recorded in transmission mode from 4000 to 400 cm^{-1} on a PerkinElmer Spectrum 100 FT-IR Spectrophotometer. Field emission scanning electron microscopy (FE-SEM) studies of samples were carried out on a FEI quanta 3D FEG-FESEM operated at 10 kV by coating the powder sample with gold. The composition of the samples was investigated by energy dispersive spectroscopy (SEM-EDS; OXFORD Instruments, INCAx-act). The transmission electron microscopy (TEM) measurements were conducted on a FEI Tecnai G^2 Spirit transmission electron microscope with acceleration voltage of 200 kV. The surface area measurements were recorded by using Quanta chrome NOVA 1200e and the surface areas of the catalysts were estimated using the BET method. UV-visible absorption spectra (UV-vis) were recorded on a THERMO Scientific Evolution 600 UV-Vis NIR spectrophotometer. X-ray photoelectron spectroscopy (XPS) was carried out on a Kratos Axis ULTRA system incorporating a 165 mm hemispherical electron energy analyzer. The photoluminescence (PL) spectra of the photocatalysts were recorded on a TSC Solutions F96pro fluorescence spectrophotometer at an excitation wavelength of 365 nm.

Photocatalytic activity

The photocatalytic activities of the synthesized samples were evaluated by the photocatalytic degradation of RhB in an aqueous solution under sunlight irradiation. Photocatalytic experiments of all the samples were conducted under similar experimental conditions in the month of April 2014 at NIT Warangal, where the fluctuation of the sunlight intensity is

minimal during this month. For comparison, we have also conducted the photocatalytic experiments under a solar simulator 300 W Xe lamp with a super cold filter (positioned 25 cm above the top of the dye suspension), which provides the visible light region ranging from 400 nm to 700 nm. The cooling water was circulated outside the photoreactor to avoid the heating effect from the radiation. In the experiment, 100 mg of photocatalyst was added into 250 mL of RhB solution with a concentration of 5 mg L^{-1}. Prior to irradiation, the solution mixture was agitated for 30 min to ensure the adsorption–desorption equilibrium between RhB molecules and photocatalyst was reached. At given irradiation time intervals, the suspensions were periodically withdrawn and centrifuged to separate the photocatalyst particulates for analysis. The filtrates were analyzed by recording variations at the wavelength of maximal absorption in the UV-vis spectrophotometer. A blank test was also conducted for the RhB aqueous solution without photocatalyst under sunlight irradiation *i.e.*, photolysis of RhB to evaluate the efficiency of the photocatalyst.

Analysis of reactive species

The effect of various reactive species on the degradation of RhB over Cr,La-codoped $SrTiO_3$ was examined to understand the photocatalytic mechanism under sunlight irradiation. The RhB solution was subjected to various scavengers prior to addition of the photocatalyst. The analysis method was similar to the photodegradation experimental process. Furthermore, the formation of hydroxyl radicals ($^{\bullet}OH$) on the surface of the sunlight irradiated photocatalyst was detected by the PL technique using terephthalic acid (TA) as a probe molecule. Terephthalic acid readily reacts with $^{\bullet}OH$ to produce a highly fluorescent product, 2-hydroxyterephthalic acid. This method relies on the PL signal generated by the hydroxylation of terephthalic acid.[26,27] In a brief experimental procedure, 0.1 g of the Cr,La-codoped $SrTiO_3$ sample was dispersed in 100 mL of a 5×10^{-4} mol L^{-1} TA aqueous solution with a 2×10^{-3} mol L^{-1} concentration of NaOH at room temperature. The resulting solution was magnetically stirred and the suspension was exposed to sunlight. At 5 min intervals, the suspension was collected and centrifuged to measure the maximum PL intensity using a fluorescence spectrophotometer with an excitation wavelength of 365 nm.

Results and discussion

The crystal structures of the synthesized pure and Cr,La-codoped $SrTiO_3$ samples were analyzed using XRD. As shown in Fig. 1a, all the diffraction peaks could be assigned to the perovskite structure having cubic symmetry (JCPDS No. 79-0176). The intensity of the diffraction peaks is decreased for Cr and La-codoped $SrTiO_3$ samples compared to pure $SrTiO_3$, which indicates the successful incorporation of Cr and La into the $SrTiO_3$ crystal structure. A careful comparison of the diffraction peaks in the range of 2θ = 32 to 33° showed that the peak positions of the Cr,La-codoped $SrTiO_3$ samples are almost the same as those of STO, since the La and Cr substitute the Sr and Ti, respectively, and the radius of La (1.032 Å) is smaller than that of Sr (1.180 Å) while the radius of Cr (0.615 Å) is bigger than that of Ti (0.605 Å).[25] The average crystallite size of all the samples was also estimated using the Scherrer equation. However, the average crystallite size was found to have decreased with an increase in Cr and La content. This is because many crystal defects form when the dopant ions occupy the regular lattice sites of $SrTiO_3$, and these defects inhibit the growth of the crystal, and thus decrease the crystal size.[28,29]

It is well known that the ideal perovskite structure is cubic with space group $Pm3m$-O_h and with a unit formula of ABO_3.[30] To evaluate the deviation of $SrTiO_3$ from the ideal situation, Goldschmidt[31] introduced a tolerance factor (t), defined by the equation: $t = (r_A + r_O)/(r_B + r_O)\sqrt{2}$ (r_A, r_B, and r_O are the empirical ionic radii at room temperature). The t values in STO, Cr,La-STO-0.5, Cr,La-STO-1.0, Cr,La-STO-1.5 and Cr,La-STO-2.0

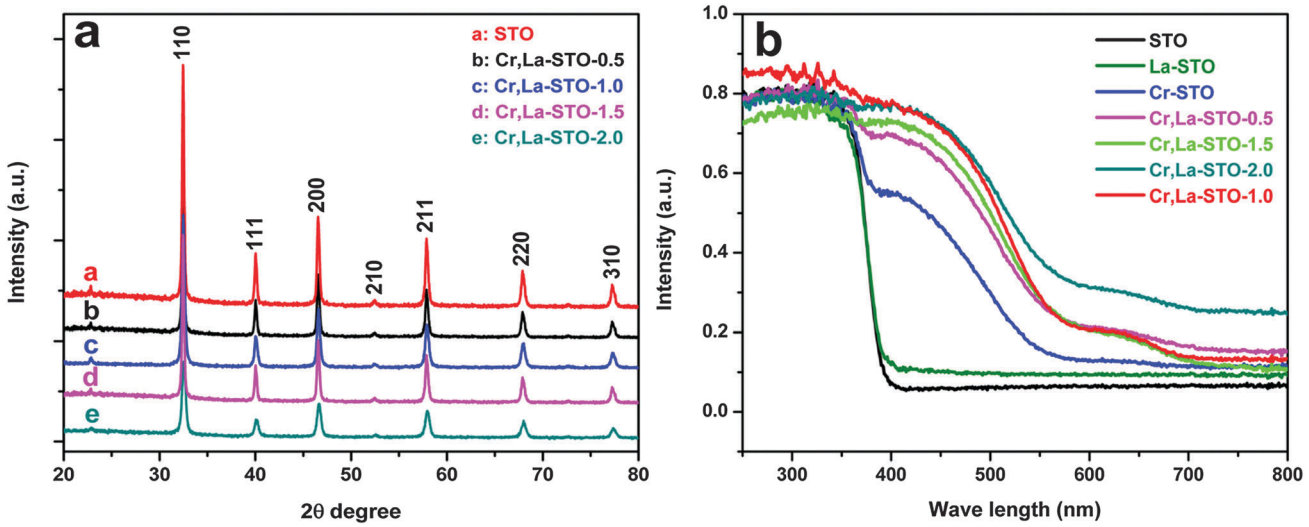

Fig. 1 (a) XRD patterns of the synthesized pure and Cr,La-codoped $SrTiO_3$ nanoparticles. (b) UV-vis diffuse reflectance spectra of all the synthesized samples.

were calculated to be 0.928, 0.917, 0.915, 0.912 and 0.909, respectively, all of which are the normally allowed t values (0.75 to 1.0).[30] So, it is further demonstrated that there is no significant distortion in the $SrTiO_3$ crystal structure.

Fig. 1b shows the absorption spectra of Cr,La-codoped $SrTiO_3$ nanoparticles determined by the diffuse reflectance measurements. For comparison, the spectra of 1 atom% La-doped $SrTiO_3$ and 1 atom% Cr-doped $SrTiO_3$ nanoparticles (synthesized by the same method, Fig. S2, ESI†) were measured and depicted in Fig. 1b. From Fig. 1b, it can be seen that the La-doped $SrTiO_3$ has an almost identical absorption edge at around 390 nm (3.12 eV) to that of pure $SrTiO_3$ (3.20 eV). Interestingly, a broad visible light absorption band, which indicates a high response to visible light, appears at around 580 nm (2.21 eV) in the UV-vis spectra of Cr-doped $SrTiO_3$. The electronic band structure of the Cr,La-codoped $SrTiO_3$ is further narrowed compared to the Cr-doped $SrTiO_3$, which is due to the large energy dispersion between the intra energy levels after codoping with La.[21,29] The absorption around 400–500 nm might be ascribed to the charge transfer from Cr^{3+} to Ti^{4+}, while the broad absorption around 580–750 nm might be ascribed to a d–d transition of $^4A_2$–$^4T_2$ in Cr^{3+}.[32,33] Moreover, the absorption spectra of Cr,La-codoped $SrTiO_3$ samples are highly dependent on the dopant concentration as shown in Fig. 1b, which exhibits obvious absorption in the visible light region. Table 1 summarizes the band gaps of the synthesized samples, which was calculated from the Kubelka–Munk functions against the photon energy (Fig. S3, ESI†).[34] The band gaps of Cr,La-codoped $SrTiO_3$ photocatalysts with a high doping amount were about 1.91 eV due to the electron transition from the electron donor levels formed by the 3d orbits of Cr^{3+} ions to the conduction band. As shown in Table 1, the values of the band gap for the synthesized samples are decreasing with an increase in the Cr and La doping content. These results suggest that the Cr^{3+} donor levels act as intermediate states for multiple photon transitions that allow electron–hole pair excitation in $SrTiO_3$ with visible light.

The FT-IR spectra of the synthesized pure and Cr,La-codoped $SrTiO_3$ samples are shown in Fig. 2. The two strong characteristic absorption bands, located at about 432 and 645 cm^{-1}, are ascribed to the vibrations of the Ti–O bonds within the TiO_6 groups, bending at a lower-frequency and stretching at a higher-frequency, respectively.[35] It is also observed that these main characteristic peaks of $SrTiO_3$ are shifted to a lower wave number region in the Cr,La-codoped $SrTiO_3$ samples as shown in Fig. 2. The red shift of these bands indicates the successful doping of Cr and La into the $SrTiO_3$ crystal structure. The broad and low intensity absorption bands observed in all the samples in the range 2850–3450 cm^{-1}, and 1618 cm^{-1} correspond to the stretching and bending vibrations of O–H groups in the physically adsorbed H_2O molecules, respectively.[36,37]

The microstructure of the synthesized Cr,La-codoped $SrTiO_3$ nanoparticles were studied using FE-SEM. Fig. 3a shows the representative FE-SEM image of the Cr,La-STO-1.0 sample. From Fig. 3a, we can see that the formed crystallites possess uniform size distribution and are homogeneous without preferentially oriented shapes. Moreover, Cr and La doping

Table 1 Physical and textural properties of the synthesized pure and Cr,La-codoped $SrTiO_3$ samples

Sample	Cr,La loading (atom%)	Actual Cr loading (from EDS) (atom%)	Actual La loading (from EDS) (atom%)	Crystallite size (nm)	Energy gap (eV)
STO	0	0	0	37	3.20
Cr,La-STO-0.5	0.5	0.45	0.37	24	1.97
Cr,La-STO-1.0	1.0	0.98	0.96	21	1.91
Cr,La-STO-1.5	1.5	1.27	1.42	22	1.92
Cr,La-STO-2.0	2.0	1.85	1.93	18	1.84

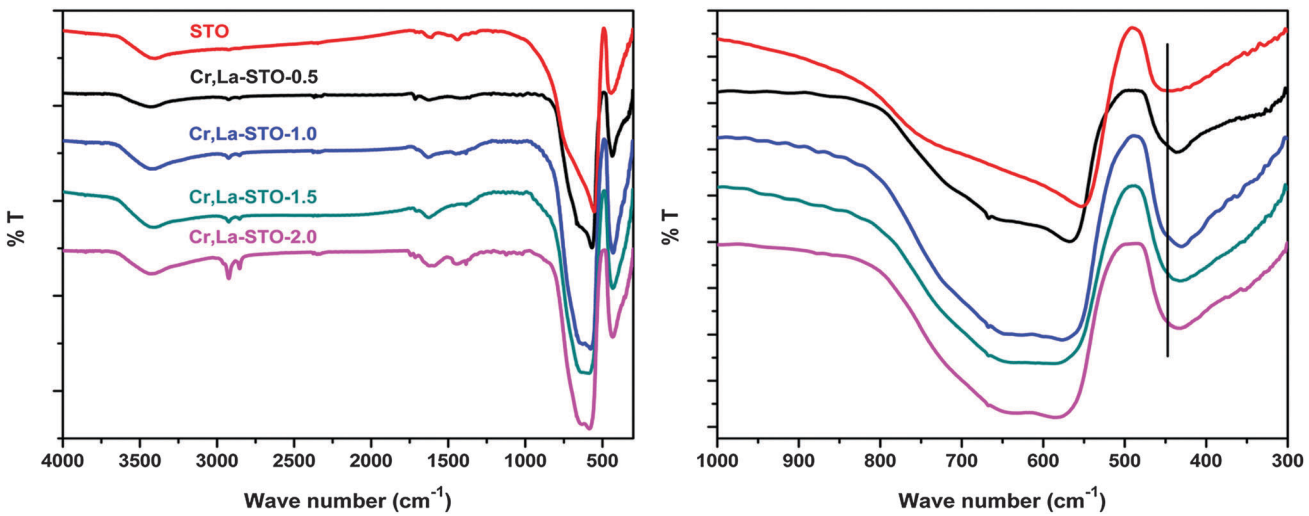

Fig. 2 FT-IR spectra of the synthesized pure and Cr,La-codoped $SrTiO_3$ nanoparticles.

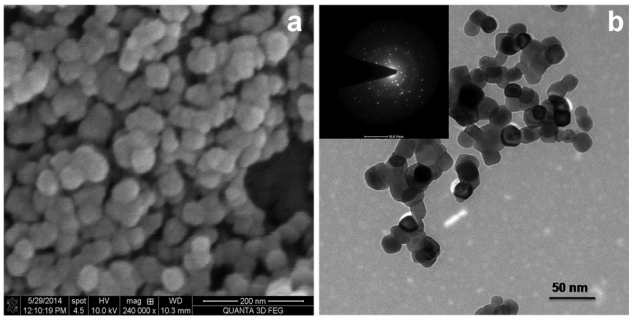

Fig. 3 (a) FE-SEM image of the synthesized Cr,La-STO-1.0 nanoparticles. (b) TEM image of the synthesized Cr,La-STO-1.0 nanoparticles, and corresponding selected area electron diffraction (SAED) pattern (inset).

concentrations in Cr,La-codoped $SrTiO_3$ nanoparticles, identified by SEM-EDS results, were similar to those initially added as shown in Fig. S4 and S5 (ESI†). These results indicate that the Cr and La ions were successfully incorporated into the crystal lattice of Cr,La-codoped $SrTiO_3$ in the present synthesis. However, the Cr and La contents in the Cr,La-codoped $SrTiO_3$ nanoparticles obtained from the EDS results are listed in Table 1.

The morphologies of the synthesized pure $SrTiO_3$ and Cr,La-codoped $SrTiO_3$ nanoparticles were characterized with TEM. All the samples show cubic morphology and their surfaces are fairly smooth. As shown in Fig. 3b, the introduction of Cr and La does not obviously change the morphology of $SrTiO_3$ nanoparticles compared with the TEM image of pure $SrTiO_3$ (Fig. S6, ESI†). The mean diameter of the pure and 1 atom% Cr,La-codoped $SrTiO_3$ nanoparticles is approximately 40 nm and 25 nm, respectively, which are in good agreement with the corresponding crystallite size calculated using the Scherrer equation. The regular crystal diffraction spots in the selected-area electron diffraction (SAED) patterns shown in the inset of Fig. 3b, reveal the single-crystalline nature of each particle for the Cr,La-STO-1.0 sample.

It is well known that the activity of a photocatalyst is also strongly influenced by the surface properties. The specific surface area of the pure $SrTiO_3$ and Cr,La-codoped $SrTiO_3$ nanoparticles was investigated by nitrogen adsorption–desorption isotherm analysis as shown in Fig. 4. The results revealed that the Cr,La-STO-1.0 sample has a surface area of about 16.85 $m^2\ g^{-1}$, which is larger than that of pure $SrTiO_3$ (8.24 $m^2\ g^{-1}$). The relatively large specific surface area of the Cr,La-codoped $SrTiO_3$ nanoparticles is useful for the better adsorption of organic molecules and also provides a greater number of reactive sites for the photocatalytic process, thereby enhancing the photocatalytic performance.[37,38]

PL studies

In order to further investigate the effect of Cr and La modification in $SrTiO_3$ on photocatalysis, PL spectra analysis was applied to reveal the migration, transfer, and recombination processes of photo-generated electron–hole pairs in semiconductors.[37] Fig. 5 shows the PL spectra of the synthesized pure and Cr,La-codoped $SrTiO_3$ nanoparticles recorded at room temperature with an excitation wavelength of 365 nm. The PL spectra of the Cr,La-codoped $SrTiO_3$ nanoparticles are similar to that of pure $SrTiO_3$ with these samples having a strong emission band centered at around 510 nm. From Fig. 5, it is also observed that there is a significant decrease in the PL intensity of Cr,La-codoped $SrTiO_3$ nanoparticles compared to that of pure $SrTiO_3$ nanoparticles. Moreover, the intensity of the PL signal for the Cr,La-STO-1.0 photocatalyst is much lower in comparison with pure $SrTiO_3$. The weak intensity PL signal indicates that the Cr,La-codoped $SrTiO_3$ photocatalysts have a lower recombination rate of photogenerated electron–hole pairs under sunlight irradiation, which is useful for greater separation of photogenerated electron–hole pairs in $SrTiO_3$.

Photocatalytic activity

The photocatalytic activity of the synthesized samples was evaluated by the degradation of an organic dye under sunlight irradiation. Rhodamine B (RhB) was chosen as a representative hazardous dye in the present work. For comparison, the

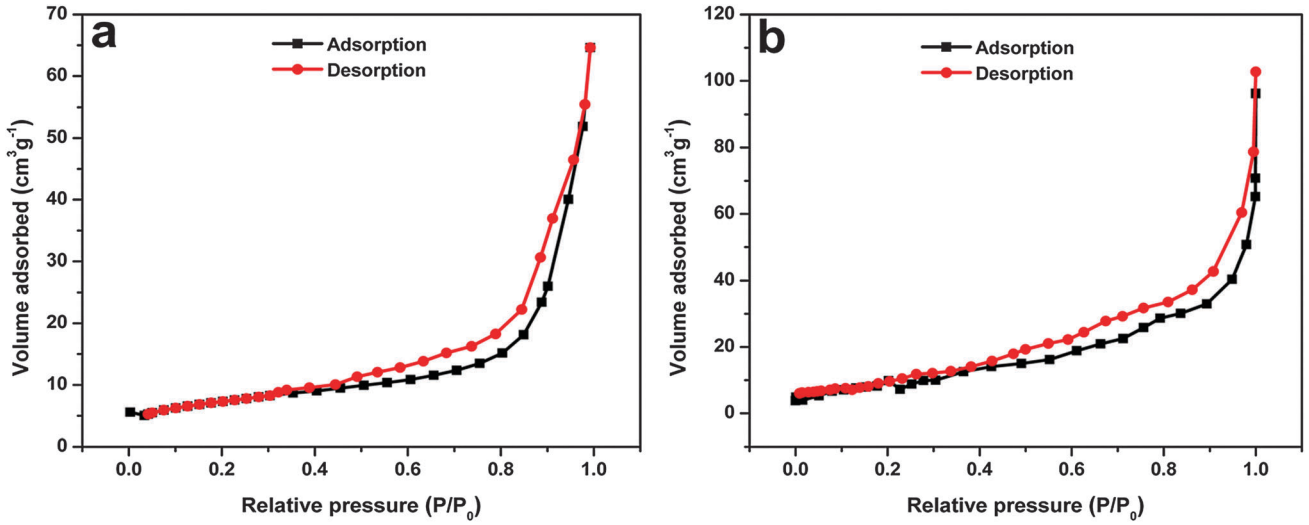

Fig. 4 Nitrogen adsorption–desorption isotherm plots for (a) pure $SrTiO_3$ and (b) Cr,La-STO-1.0 nanoparticles.

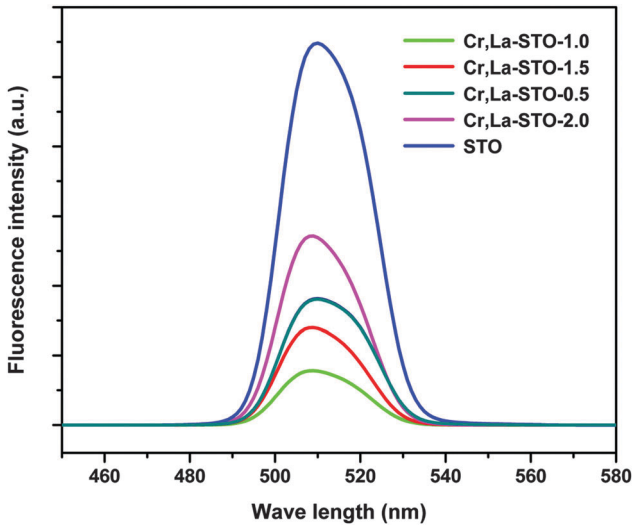

Fig. 5 Room temperature PL spectra of the synthesized pure and Cr,La-codoped $SrTiO_3$ nanoparticles excited at 365 nm.

photolysis of RhB dye (without catalyst) and adsorption ability of the catalyst (in absence of sunlight) for the same duration under the same experimental conditions were also investigated. These results suggest that both light and catalyst are necessary for an efficient photocatalytic degradation reaction. The time for RhB degradation in different catalyst systems are shown in Fig. 6a. It is interesting that the pure $SrTiO_3$, which is almost inactive in the visible region due to a high band gap (3.2 eV), also gave some degradation of RhB due to the sensitization mechanism of photocatalysis.[39] According to the dye sensitization mechanism the RhB molecules adsorbed on the surface of catalysts can be excited by sunlight irradiation. The electron from the excited dye molecule is rapidly injected into the conduction band of the $SrTiO_3$, and the formed radicals at the surface undergo dye degradation quickly.[40] As can be seen from Fig. 6a, the synthesized Cr and La-codoped $SrTiO_3$ photocatalysts exhibit a much higher photocatalytic activity than pure $SrTiO_3$. These results also demonstrate that the doping amount of Cr and La has a strong influence on the photodegradation of RhB. Thus, the optimal Cr and La content in $SrTiO_3$ is 1 atom%, and then the photocatalytic activity decreases with increasing Cr and La content. The decrease in the photocatalytic activity can be attributed to the fact that excess dopant species may act as recombination centers for photo-induced electron–hole pairs, thereby reducing the efficiency of charge separation.[29] The corresponding first-order kinetics plot shown in Fig. 6b indicates that the Cr,La-STO-1.0 nanoparticles exhibit the highest degradation rate, which is almost 6 times higher than that of pure $SrTiO_3$ and 3 times higher than that of Cr-doped $SrTiO_3$ nanoparticles. Furthermore, the photocatalytic activity of the synthesized catalysts for the degradation of RhB was also investigated under visible light irradiation. The efficiency of the photolysis of RhB was negligible under the same experimental conditions, which indicated that the RhB is stable under visible light irradiation. Notably, the photocatalytic activity of pure $SrTiO_3$ under visible light irradiation is much lower compared to the activity under sunlight irradiation as shown in Fig. S7 (ESI†). However, the photocatalytic activity of the Cr,La-codoped $SrTiO_3$ photocatalysts under visible light irradiation is slightly lower compared to the activity under direct sunlight illumination but it is much higher than that of pure $SrTiO_3$, La-doped $SrTiO_3$ and Cr-doped $SrTiO_3$ nanoparticles.

According to theoretical investigations,[20,41,42] the valence band maximum (VBM) of $SrTiO_3$ is mainly composed of the nonbonding O 2p orbitals whereas the conduction band minimum (CBM) is merely the contribution of the Ti 3d orbitals. Moreover, the Sr 3d orbitals contribute very little to both the valence band and the lower part of conduction band. On the other hand, the Cr-doped $SrTiO_3$ shows high photocatalytic activity compared to pure $SrTiO_3$ due to the formation of new energy states introduced by the Cr 3d

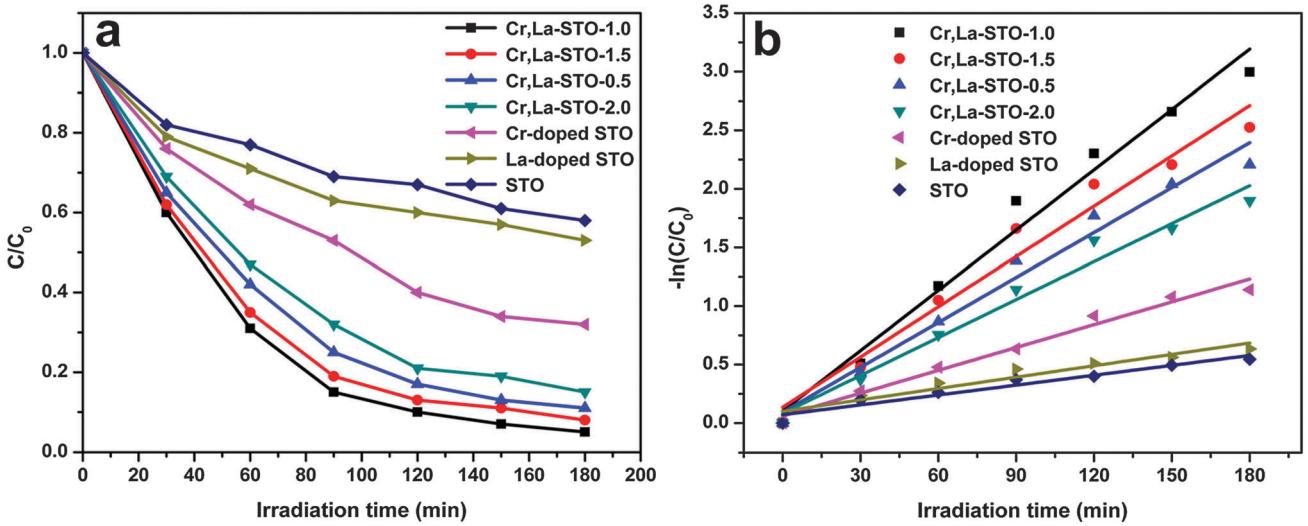

Fig. 6 (a) Comparison of photocatalytic activity for the degradation of RhB in aqueous solution under sunlight irradiation over pure and Cr,La-codoped $SrTiO_3$ nanoparticles and (b) the corresponding first-order kinetics plot of pure and Cr,La-codoped $SrTiO_3$ nanoparticles.

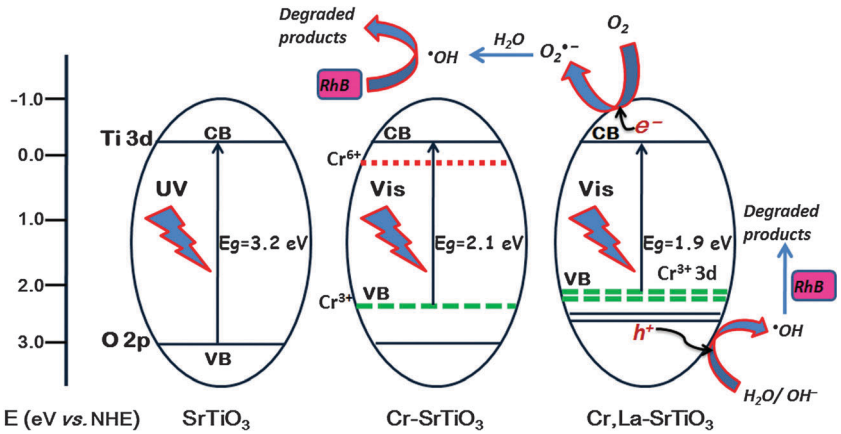

Fig. 7 Schematic illustration of the high photocatalytic activity of Cr,La-codoped $SrTiO_3$ nanoparticles for the degradation of RhB in aqueous solution under sunlight irradiation.

orbitals which lie above the VBM (Fig. 7). Thus, the minimum energy gap is reduced because the excitation energy of the electrons in these states is lower than that of the O 2p electrons. For comparison, photodegradation of RhB over 1 atom% La-doped $SrTiO_3$ and 1 atom% Cr-doped $SrTiO_3$ photocatalysts were also carried out. The photodegradation results show that La-doped $SrTiO_3$ nanoparticles display a very low activity, which is close to that of the pure $SrTiO_3$, whereas Cr-doped $SrTiO_3$ nanoparticles exhibit a higher activity as shown in Fig. 6a. It is obvious that the Cr-doping enhances the photocatalytic activity, while the La-mono doping is almost non-effective because it does not reduce the band gap of $SrTiO_3$, which is also confirmed by UV-vis DRS studies. However, the synthesized Cr,La-codoped $SrTiO_3$ samples show a much higher activity compared to Cr-doped $SrTiO_3$ for the photodegradation of RhB under the same conditions. This is because, only Cr substituting for Ti with a +3 oxidation state accounts for such visible light activity for Cr-doped $SrTiO_3$, while Cr substituting for Ti with +6 oxidation state, will act as a recombination centre for photogenerated electron–hole pairs. After La incorporation into the Cr-doped $SrTiO_3$ structure, one excess electron is released to compensate for Cr^{3+} in Cr,La-codoped $SrTiO_3$ as La is mainly a substitute for Sr but not Ti.[25,43] The expanding light absorption region can also effectively improve the photocatalytic activity of Cr,La-codoped $SrTiO_3$. More importantly, the synthesized Cr,La-codoped $SrTiO_3$ nanoparticles have a high surface area which is almost twice that of the pure $SrTiO_3$ and smaller in crystallite size. From the aforementioned results, we can conclude that the synthesized Cr,La-codoped $SrTiO_3$ photocatalysts display the highest photocatalytic activity for the degradation of RhB under sunlight irradiation.

Trapping experiment

Although the above mentioned results and analyses have revealed that the incorporated Cr and La ions could change the physico-chemical properties such as band structure and surface area of $SrTiO_3$, and thus improve the photocatalytic activity of Cr and La-codoped $SrTiO_3$ photocatalysts, it is not clear about the reactive species which are mainly responsible for the degradation of RhB under sunlight irradiation. To answer this question, we studied the role of main reactive species including hydroxyl radicals (•OH), superoxide anion radicals ($O_2^{\bullet-}$) and holes (h^+), in the degradation of RhB under sunlight irradiation over Cr and La-codoped $SrTiO_3$ nanoparticles, by performing a radical trapping experiment. To confirm the role of these reactive species, different scavengers, namely ammonium oxalate (AO) for h^+, *tert*-butyl alcohol (TBA) for •OH and N_2 for $O_2^{\bullet-}$, were employed in this study.[37,44] As can be seen from Fig. 8a, the photocatalytic degradation of RhB decreases most rapidly after the addition of TBA, indicate that •OH was the major reactive species during degradation of RhB in the Cr and La-codoped $SrTiO_3$ system. It was also observed that the degradation of RhB was inhibited by the addition of AO (an efficient trapper of holes), which is significant but does not lead to complete quenching of the reaction (Fig. 8a). In addition, a very small change in the degradation of RhB is observed after N_2 purging was conducted. These results confirm that photogenerated •OH and h^+ play an important role in the degradation of RhB.

Hydroxyl radical generation

It has been widely accepted that hydroxyl radicals (•OH) are the main reactive species responsible for the degradation of organic pollutants under light irradiation. The •OH generation during the photocatalytic process can be easily detected by a PL technique using terephthalic acid (TA) as a probe molecule. The •OH reacts with terephthalic acid in a basic solution to generate 2-hydroxyterephthalic acid which emits a unique fluorescence signal with its peak centered at around 425 nm. As shown in Fig. 8b, significant fluorescence signals associated with 2-hydroxyterephthalic acid were generated upon sunlight irradiation of the Cr,La-codoped $SrTiO_3$ photocatalysts suspended in a TA solution at different irradiation times. These results confirm that the fluorescence is caused by chemical reactions of terephthalic acid with •OH formed on the surface of the Cr,La-codoped $SrTiO_3$ photocatalysts *via* photocatalytic reactions.[26,45]

Reusability

In addition to photocatalytic efficiency, the reusability of a photocatalyst is also very important for practical applications.

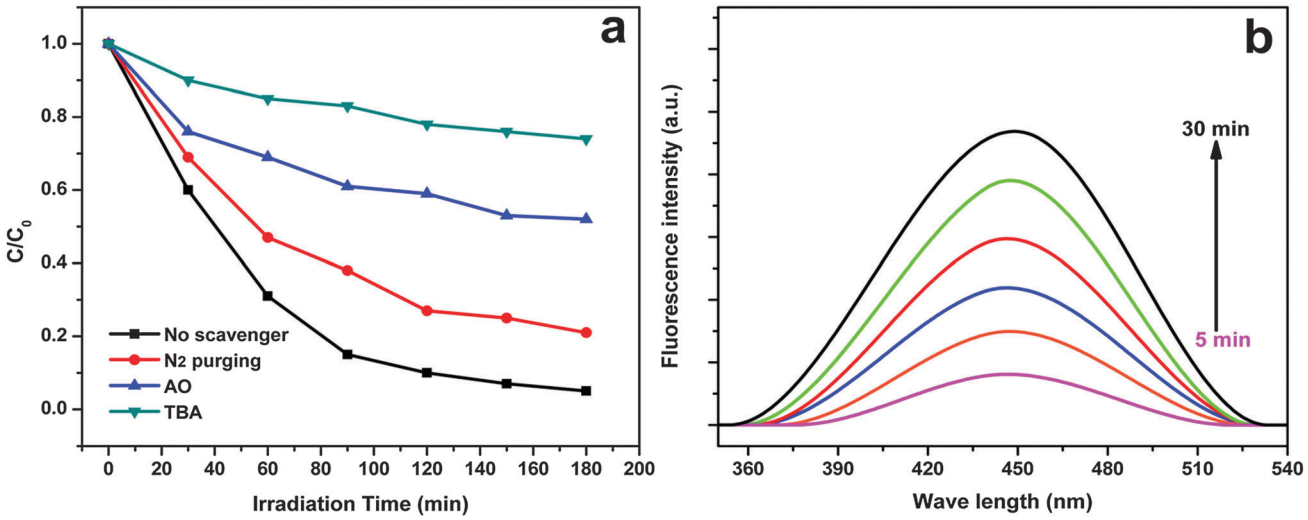

Fig. 8 (a) Effect of different scavengers on the degradation of RhB in the presence of the Cr,La-STO-1.0 photocatalyst under sunlight irradiation and (b) •OH trapping PL spectra of Cr,La-STO-1.0 with TA solution under sunlight irradiation.

To evaluate the reusability of Cr,La-codoped $SrTiO_3$ nanoparticles, five successive photocatalytic experimental runs were conducted by adding recycled Cr,La-STO-1.0 photocatalyst to fresh RhB solutions with no change in the overall concentration of the catalyst under sunlight irradiation. As shown in Fig. 9a, it is found that the photocatalytic activity of the Cr,La-STO-1.0 sample does not exhibit a significant loss after five recycles for the photodegradation of RhB. Moreover, the XRD pattern (Fig. 9b) of the reused sample also illustrated that the crystal structure of the Cr,La-STO-1.0 photocatalysts did not change after the photocatalytic reaction, which indicates that the synthesized Cr,La-codoped $SrTiO_3$ nanoparticles can be used as a reusable photocatalyst for photocatalytic oxidation of pollutant molecules.

In addition, XPS measurements were also performed to investigate the oxidation state of Cr in Cr-doped $SrTiO_3$ and Cr,La-codoped $SrTiO_3$ nanoparticles before and after the photocatalytic experiments. As shown in Fig. 10, the Cr,La-STO-1.0 photocatalyst shows the sharp peak at about 576.3 eV, which could be assigned to Cr^{3+}, indicating that the oxidation state of Cr didn't change after the photocatalytic reaction. The Cr-doped $SrTiO_3$ sample showed a relatively low peak intensity of Cr^{3+}, and a small shoulder peak assigned to Cr^{6+} at 579.2 eV was also observed,[15] however, a high concentration of Cr^{6+} was observed after the photocatalytic reaction. Therefore, the results of XPS allow us to understand the effect of the codopant on the oxidation state of the doped Cr, which strongly influences the photocatalytic activity of Cr,La-codoped $SrTiO_3$ photocatalysts.

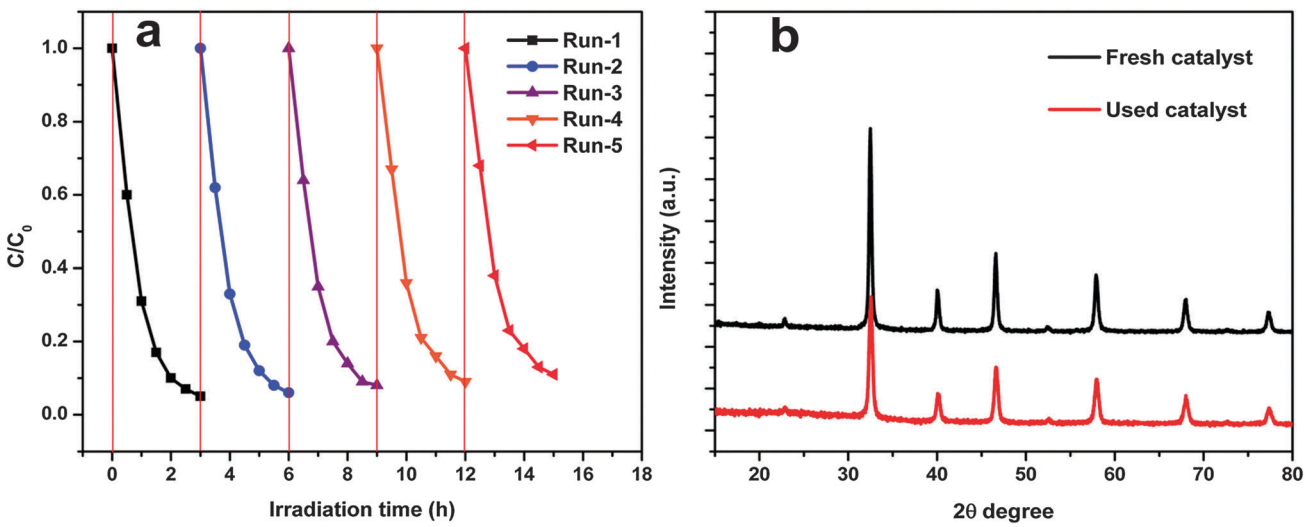

Fig. 9 (a) Reusability of the Cr,La-STO-1.0 photocatalyst in five successive experimental runs for the photocatalytic degradation of RhB in aqueous solution under sunlight irradiation. (b) XRD patterns of the synthesized Cr,La-STO-1.0 photocatalyst before and after the cycling photocatalytic experiments.

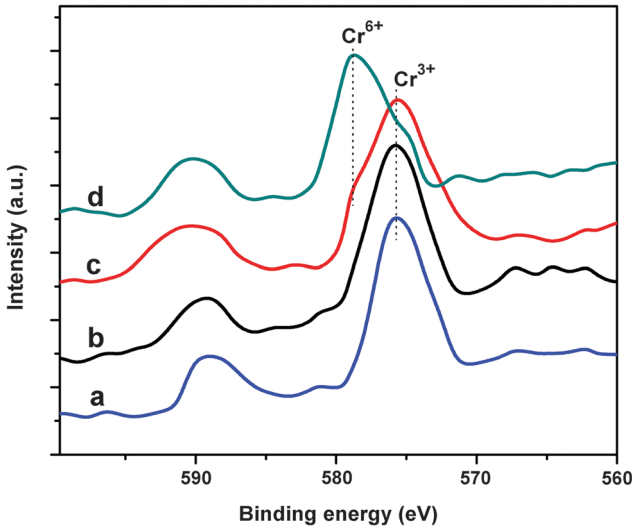

Fig. 10 XPS spectra of Cr 2p in the Cr,La-STO-1.0 photocatalyst before (a), and after (b) the photocatalytic reaction; and Cr 2p in the Cr-doped STO photocatalyst before (c), and after (d) the photocatalytic reaction.

Conclusion

In summary, Cr,La-codoped $SrTiO_3$ nanoparticles have been successfully synthesized *via* a polymeric citrate precursor method. The band structure, crystal size and surface area of $SrTiO_3$ were significantly affected after the introduction of Cr and La into the $SrTiO_3$ crystal structure. The Cr,La-codoped $SrTiO_3$ nanoparticles exhibited an enhanced photocatalytic activity for the degradation of RhB under sunlight irradiation. The photocatalytic results revealed that the charge state of Cr plays an important role in the improved photocatalytic activity of Cr,La-codoped $SrTiO_3$ nanoparticles. The enhanced photocatalytic performance of Cr,La-codoped $SrTiO_3$ nanoparticles under sunlight irradiation is due to synergistic effects including a high visible light response, a significant decrease in crystal size, and a high surface area. In addition, the trapping experiments confirmed that photogenerated $^{\bullet}OH$ and h^+ are the major reactive species responsible for the photodegradation of RhB in the Cr,La-codoped $SrTiO_3$ system. Therefore, the present work demonstrates that the codoping strategy can be useful in the design and development of advanced photocatalytic materials for environmental remediation.

Acknowledgements

Authors thank the Department of Science and Technology, Government of India for financial support (SR/FT/CS-096/2009). Surendar Tonda also thanks the Ministry of Human Resource Development, Government of India, for providing a fellowship.

References

1 H. Tong, S. X. Ouyang, Y. P. Bi, N. Umezawa, M. Oshikiri and J. H. Ye, *Adv. Mater.*, 2012, **24**, 229–251.
2 M. R. Hoffmann, S. T. Martin, W. Y. Choi and D. W. Bahnemann, *Chem. Rev.*, 1995, **95**, 69–96.
3 H. L. Zhou, Y. Q. Qu, T. Zeida and X. F. Duan, *Energy Environ. Sci.*, 2012, **5**, 6732–6743.
4 A. Kudo and Y. Miseki, *Chem. Soc. Rev.*, 2009, **38**, 253–278.
5 Z. Zou, J. Ye, K. Sayama and H. Arakawa, *Nature*, 2001, **414**, 625–627.
6 A. Fujishima and K. Honda, *Nature*, 1972, **238**, 37–38.
7 K. Rajeshwara, M. E. Osugib, W. Chanmaneec, C. R. Chenthamarakshana, M. V. B. Zanonib, P. Kajitvichyanukuld and R. Krishnan-Ayera, *J. Photochem. Photobiol., C*, 2008, **9**, 171–192.
8 M. S. Wrighton, A. B. Ellis, P. T. Wolczanski, D. L. Morse, H. B. Abrahamson and D. S. Ginley, *J. Am. Chem. Soc.*, 1976, **98**, 2774–2779.
9 A. K. Ghosh and H. P. Maruska, *J. Electrochem. Soc.*, 1977, **124**, 1516–1522.
10 K. Domen, S. Naito, T. Onishi, K. Tamaru and M. Soma, *J. Phys. Chem.*, 1982, **86**, 3657–3661.
11 T. K. Townsend, N. D. Browning and F. E. Osterloh, *ACS Nano*, 2012, **6**, 7420–7426.
12 T. K. Townsend, N. D. Browning and F. E. Osterloh, *Energy Environ. Sci.*, 2012, **5**, 9543–9550.
13 S. Hara, M. Yoshimizu, S. Tanigawa, L. Ni, B. Ohtani and H. Irie, *J. Phys. Chem. C*, 2012, **116**, 17458–17463.
14 H. P. Maruska and A. K. Ghosh, *Sol. Energy Mater.*, 1979, **1**, 237–247.
15 H. Kato and A. Kudo, *J. Phys. Chem. B*, 2002, **106**, 5029–5034.
16 L. F. da Silva, J. C. M'Peko, J. Andres, A. Beltran, L. Gracia, M. I. B. Bernardi, A. Mesquita, E. Antonelli, M. L. Moreira and V. R. Mastelaro, *J. Phys. Chem. C*, 2014, **118**, 4930–4940.
17 T. Umebayashi, T. Yamaki, H. Itoh and K. Asai, *J. Phys. Chem. Solids*, 2002, **63**, 1909–1920.
18 D. Wang, J. Ye, T. Kako and T. Kimura, *J. Phys. Chem. B*, 2006, **110**, 15824–15830.
19 H. Yu, S. Ouyang, S. Yan, Z. Li, T. Yu and Z. Zou, *J. Mater. Chem.*, 2011, **21**, 11347–11351.
20 P. Reunchan, N. Umezawa, S. Ouyang and J. Ye, *Phys. Chem. Chem. Phys.*, 2012, **14**, 1876–1880.
21 H. Yu, S. Yan, Z. Li, T. Yu and Z. Zou, *Int. J. Hydrogen Energy*, 2012, **37**, 12120–12127.
22 M. J. P. Park, K. Burk and M. Ernzerhof, *Phys. Rev. Lett.*, 1996, **77**, 3865–3868.
23 Y. Jia, S. Shen, D. Wang, X. Wang, J. Shi, F. Zhang, H. Han and C. Li, *J. Mater. Chem. A*, 2013, **1**, 7905–7912.
24 T. Ishii, H. Kato and A. Kudo, *J. Photochem. Photobiol., A*, 2004, **163**, 181–186.
25 S. X. Ouyang, H. Tong, N. Umezawa, J. Cao, P. Li, Y. Bi, Y. Zhang and J. Ye, *J. Am. Chem. Soc.*, 2012, **134**, 1974–1977.
26 K. Ishibashi, A. Fujishima, T. Watanabe and K. Hashimoto, *Electrochem. Commun.*, 2000, **2**, 207–210.
27 S. Liu, C. Li, J. Yu and Q. Xiang, *CrystEngComm*, 2011, **13**, 2533–2541.
28 J. Mrazek, L. Spanhel, G. Chadeyron and V. Matejec, *J. Phys. Chem. C*, 2010, **114**, 2843–2852.
29 T. Surendar, S. Kumar and V. Shanker, *Phys. Chem. Chem. Phys.*, 2014, **16**, 728–735.

30 M. A. Pena and J. L. G. Fierro, *Chem. Rev.*, 2001, **101**, 1981–2018.
31 V. M. Goldschmidt, *Skr. Nor. Viedenk.-Akad. Kl. I: Mater.-Naturvidensk. Kl*, 8, 1926.
32 J. W. Liu, G. Chen, Z. H. Li and Z. G. Zhang, *J. Solid State Chem.*, 2006, **179**, 3704–3708.
33 D. W. Hwang, H. G. Kim, J. S. Lee, J. Kim, W. Li and S. H. Oh, *J. Phys. Chem. B*, 2005, **109**, 2093–2102.
34 H. Irie, Y. Maruyama and K. Hashimoto, *J. Phys. Chem. C*, 2007, **111**, 1847–1852.
35 P. Jayabal, V. Sasirekha, J. Mayandi, K. Jeganathan and V. Ramakrishnan, *J. Alloys Compd.*, 2014, **586**, 456–461.
36 V. Elia, G. Ausanio, A. De Ninno, F. Gentile, R. Germano, E. Napoli and M. Niccoli, *Water*, 2013, **5**, 16–26.
37 S. Kumar, T. Surendar, A. Baruah and V. Shanker, *J. Mater. Chem. A*, 2013, **1**, 5333–5340.
38 Y. Wang, R. Shi, J. Lin and Y. Zhu, *Energy Environ. Sci.*, 2011, **4**, 2922–2929.
39 A. Z. Jia, X. Q. Liang, Z. Q. Su, T. Zhu and S. X. Liu, *J. Hazard. Mater.*, 2010, **178**, 233–242.
40 M. Miyauchi, M. Takashio and H. Tobimastsu, *Langmuir*, 2004, **20**, 232–236.
41 H. C. Chen, C. W. Huang, J. C. S. Wu and S. T. Lin, *J. Phys. Chem. C*, 2012, **116**, 7897–7903.
42 P. Reunchan, S. Ouyang, N. Umezawa, H. Xu, Y. Zhang and J. Ye, *J. Mater. Chem. A*, 2013, **1**, 4221–4227.
43 J. Wang, T. Fang, S. Yan, Z. Li, T. Yu and Z. Zou, *Comput. Mater. Sci.*, 2013, **79**, 87–94.
44 S. Kumar, A. Baruah, T. Surendar, B. Kumar, V. Shanker and B. Sreedhar, *Nanoscale*, 2014, **6**, 4830–4842.
45 J. Yu, W. Wang, B. Cheng and B. L. Su, *J. Phys. Chem. C*, 2009, **113**, 6743–6750.

